Contents lists available at ScienceDirect

Chemical Engineering Research and Design

journal homepage: www.elsevier.com/locate/cherd

Pressure drop, void fraction and flow pattern of vertical air–silicone oil flows using differential pressure transducer and advanced instrumentation

M. Abdulkadir[a,*], D.G. Jatto[b], L.A. Abdulkareem[c], D. Zhao[d]

[a] Chemical Engineering Department, Federal University of Technology, Minna, Niger State, Nigeria
[b] Petroleum Engineering Department, African University of Science and Technology, Abuja, Nigeria
[c] Petroleum Engineering Department, College of Engineering, University of Zakho, Iraq
[d] School of Engineering, London South Bank University, London, United Kingdom

ARTICLE INFO

Article history:
Received 23 November 2019
Received in revised form 1 March 2020
Accepted 6 April 2020
Available online 17 April 2020

Keywords:
Void fraction
Pressure gradient
Flow pattern
Prediction
DP cell

ABSTRACT

New data for pressure drop, void fraction and flow pattern in a vertical riser using air–silicone oil as the system fluid are reported in this work. A differential pressure cell (DP cell) was used to measure the pressure drop. Also, void fraction data were recorded simultaneously by an electrical capacitance tomography (ECT) and wire mesh sensor (WMS). The observed flow patterns are the spherical cap bubble, slug and churn flows. However, only the slug flow without the presence of churn flow is seen within the transition line as predicted by the map. The characteristic probability density function (PDF) derived from void fraction data was used to determine the flow patterns. A comparison between present experimental results and the air–water data reported in the literature was carried out and various levels of agreement were achieved. The PDFs obtained from the DP cell signals for spherical cap bubble and slug flows significantly differ from those derived from the ECT and WMS outputs. Current void fraction and pressure gradient results were compared with the values predicted by ten empirical correlations selected from the literature. Statistical tools such as Mean Square Error (MSE), Root Mean Square Error (RMSE) and Mean Absolute Percentage Error (MAPE) were applied in the comparison. The Greskovich and Cooper correlation gave the least MSE, RMSE and MAPE values of 0.0007908, 0.013 and 3.05%, respectively for slug flow.

1. Introduction

The simultaneous flow of liquid and gas otherwise known as two-phase gas–liquid flow is a common occurrence in power generation in nuclear plants, oil and gas and chemical processes (Abdulkadir [1]). For several decades, a considerable amount of effort has been dedicated by many researchers to understanding and confronting the underlying physics of two-phase gas–liquid flow phenomena. It is worth mentioning that it is unfeasible to appreciate gas–liquid flow phenomena without a clear understanding of the flow patterns encountered. It is anticipated that the flow patterns will impact the void fraction or liquid holdup, pressure drop, heat and mass transfer during the heat and mass transfer processes. The ability to accurately determine the flow pattern is essential before related calculation procedures can be established. Conversely, most of the flow pattern transition criteria were developed for air–water system and small diameter pipes, hence the accuracy can be uncertain when the criteria are applied to modelling of two-phase flow in medium or large diameter pipes. A small diameter pipe according to Wang et al. (2012) and Waltrich et al. (2013) is 9-55 mm, 67 mm is defined as medium pipe diameter according to Azzopardi et al. (2015) and a large diameter according to Omebere-Iyari and Azzopardi (2007), Ali (2009), van der Meulen (2012) and Abdulkadir et al. (2019) is 127 mm.

* Corresponding author.
E-mail address: mukhau@futminna.edu.ng (M. Abdulkadir).
https://doi.org/10.1016/j.cherd.2020.04.009

A substantial number of studies have been carried out and are still ongoing to accurately predict flow pattern. Some of the early works concerned with the determination of flow patterns include that of Nichols (1965), Wallis (1969), Govier and Aziz (1972), Crawford (1983), Mandhane et al. (1974), Nguyen (1975), Yamazaki and Yamaguchi (1979), Mukherjee (1979), Taitel et al. (1980), Su and Metcalfe (1997), Omebere-lyari and Azzopardi (2000), Furukawa and Fukano (2001) and Hanratty et al. (2003). One common feature from the findings of these researchers is the fact that gas–liquid flow is a complex phenomenon and that the complex nature of these flows gave rise to what is called flow patterns. They concluded that the flow pattern is influenced by several flow parameters such as void fraction and pressure drop amongst others. The common flow patterns found in vertical gas–liquid are as follows:

Bubbly flow: In bubbly flow, the gas phase is distributed as discrete bubbles in the continuous liquid phase, as shown in Fig. 1a. The number of bubbles increases with an increase in gas superficial velocity and thus, collisions between the bubbles occur more often. This accounts for a rise in the observed bubble coalescence.

Spherical cap bubble flow: In this flow regime shown in Fig. 1b, there are swarms of small bubbles as the gas superficial velocity increases. These bubbles in time form larger ones, but not big enough to cover the pipe diameter. As a result, of coalescence and velocity differences, the bubbles are not uniformly distributed along the pipe. Slug flow: Is a flow pattern that is categorized by large bullet-shaped bubbles as shown in Fig. 1c which occupy approximately the whole cross-section of the tube. These bubbles are surrounded by a thin film of falling liquid and are separated from each other by regions of liquid, otherwise called liquid slugs. These liquid slugs may or may not contain small gas bubbles. Churn flow: Is a highly disturbed flow of gas and liquid in which an increase in the gas superficial velocity causes the liquid slug to become unstable, leading to break-up and fall. This liquid merges with the approaching slug, which then resumes its upward motion until it becomes unstable and after which it falls once again, as shown in Fig. 1d. Annular flow: This flow pattern represented in Fig. 1e is categorized by a central core of fast-flowing gas and a slower moving liquid film that moves around the pipe wall. In this flow pattern, small amplitude waves, known as ripple waves, are produced on the liquid surface owing to the shearing action of the gas at the gas–liquid interface.

Spherical cap bubble flow: In this flow regime shown in Fig. 1b, there are swarms of small bubbles as the gas superficial velocity increases. These bubbles in time form larger ones, but not big enough to cover the pipe diameter. As a result, of coalescence and velocity differences, the bubbles are not uniformly distributed along the pipe.

Slug flow: Is a flow pattern that is categorized by large bullet-shaped bubbles as shown in Fig. 1c which occupy approximately the whole cross-section of the tube. These bubbles are surrounded by a thin film of falling liquid and are separated from each other by regions of liquid, otherwise called liquid slugs. These liquid slugs may or may not contain small gas bubbles.

Churn flow: Is a highly disturbed flow of gas and liquid in which an increase in the gas superficial velocity causes the liquid slug to become unstable, leading to break-up and fall. This liquid merges with the approaching slug, which then resumes its upward motion until it becomes unstable and after which it falls once again, as shown in Fig. 1d. Annular flow: This flow pattern represented in Fig. 1e is categorized by a central core of fast-flowing gas and a slower moving liquid film that moves around the pipe wall. In this flow pattern, small amplitude waves, known as ripple waves, are produced on the liquid surface owing to the shearing action of the gas at the gas–liquid interface.

On the matter of industrial applications where the flow of a mixture of two or more phases can occur, the task of sizing the equipment for gathering, pumping and transporting of such phases requires the challenging task of determining the void fraction based on the prevailing operating conditions. Void fraction describes the volumetric gas fraction and is an important parameter for hydrodynamic and thermal design in various two-phase gas–liquid systems. A vast number of studies have been carried out and are still ongoing to accurately predict the void fraction. Notable amongst them are Sokolov et al. (1969), Beggs (1972), Clark and Flemmer (1985), Spedding et al. (1990), Yijun and Rezkallah (1993), Woldesemayat and Ghajar (2007), Bhagwat and Ghajar (2014) and Abdulkadir et al. (2014a, 2018). Owing to the complexity and lack of understanding of the basic underlining physics of the problem, the majority of the analyses are more motivated towards empirical correlations. The harsh truth is that most of the void fraction empirical correlations are restricted to air–water or steam–water flow in pipes, and the correlations that are specifically established for liquids with a higher viscosity than water are relatively scarce.

Because the accuracy of pressure drop prediction in flowing wells has a significant influence on the fluid flow measurement, the two-phase pressure drop prediction using empirical correlations has been investigated by Lockhart and Martinelli (1949), Orkiszewski (1967), Chisholm (1973) and Friedel (1979). The empirical correlations are valid only for some specific conditions. This is due to the complexity of two-phase flow analysis. In some conditions, owing to the slippage between the gas and the liquid phases, the gas travels at a much higher velocity than the liquid. The determination of the mixture density depends on the accuracy of the void fraction or liquid holdup. Also, the flow velocity and flow pattern need to be known a priori in most pressure drop prediction. Unfortunately, it is still a problem to design a combination sensor system for correctly determining flow pattern, void fraction and pressure drop of an air–silicone oil flow in a vertical pipe. According to Griffith (1962), the difference in velocity and flow pattern of the two phases strongly affect pressure gradient computations.

In this study, a combination of the differential pressure transducer and advanced instrumentation, electrical capacitance tomography (ECT), wire mesh sensor (WMS) were deployed to measure pressure drop, void fraction and flow pattern in vertical air–silicone oil flows. A comparison between the present experimental void fraction data involving air–silicone oil was made against reported air–water data of Hernandez-Perez (2008). Also, the measured pressure drop, void fraction and flow pattern were compared against available models reported in the literature. The comparison was with consideration for flow patterns to confirm whether or not the candidate model can be applied to a nearly universal database, at least dealing with vertical upflows. Determination of the fluid flow phenomena inside the medium-large diameter pipe using a liquid with a viscosity 5.25 times that of water and improving the prediction accuracy of pressure

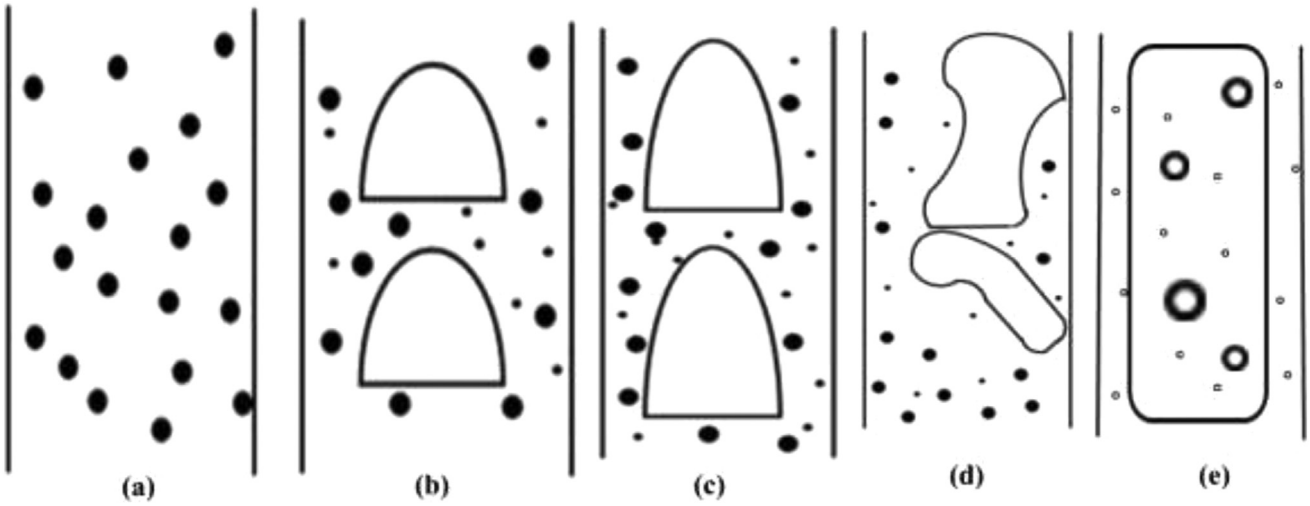

Fig. 1 – Typical flow patterns in a vertical gas–liquid flow: (a) bubbly flow; (b) spherical cap bubble flow; (c) slug flow; (d) churn flow and (e) annular flow.

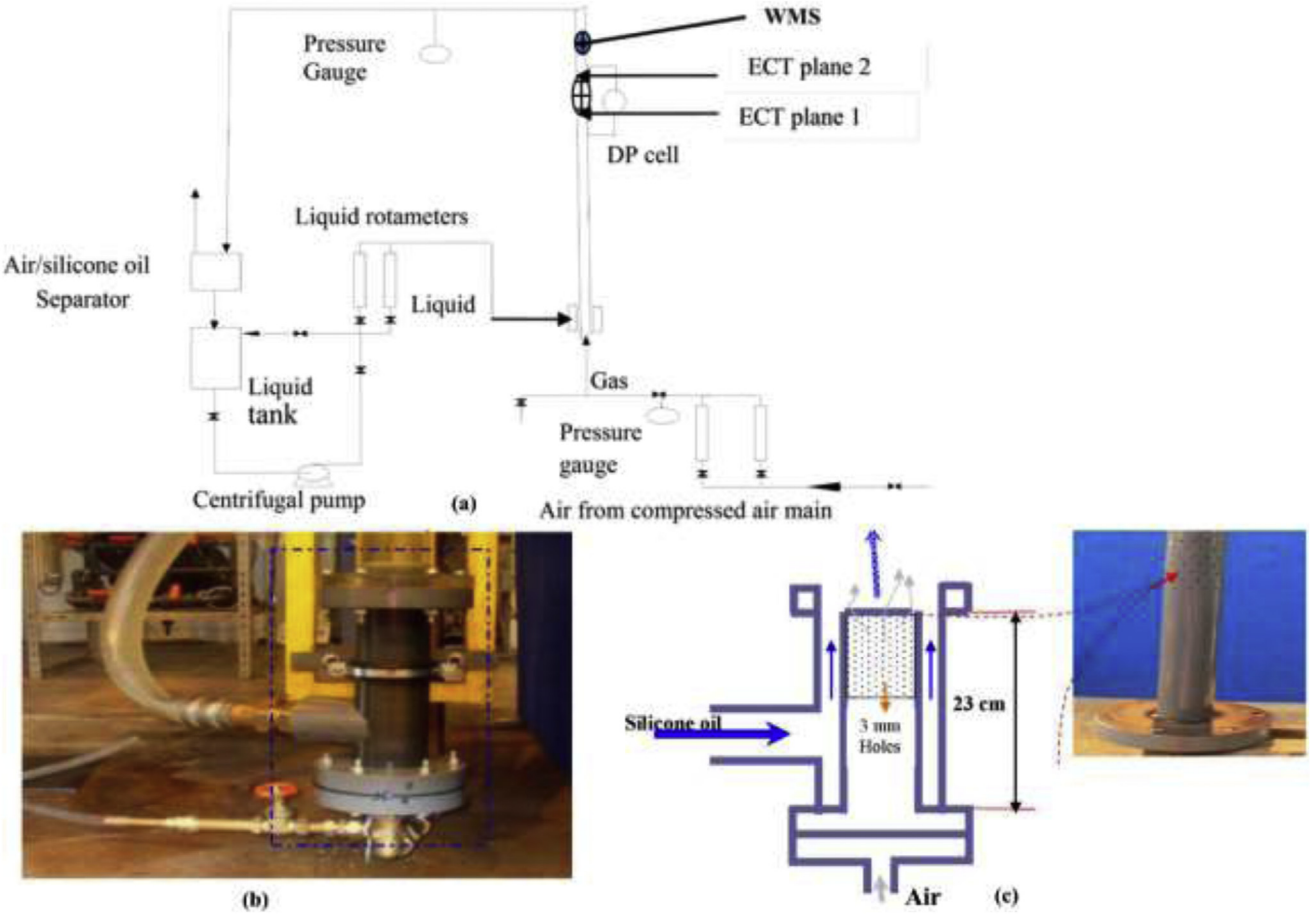

Fig. 2 – (a) Experimental facility employed in this work. The exact measurement locations of the ECT plane 1, ECT plane 2 and WMS are 4.4, 4.489 and 4.92 m, respectively. On the other hand, the exact measurement locations for the DP cell are 4.5 and 5.36 m; (b) picture of the gas–liquid mixing section; (c) schematic diagram of the gas–liquid mixing section including the porous pipe section.

drop, flow pattern and void fraction are important in particular for applications involving hydrocarbon transportation. It is worthy of mention that this work is also devoted to supporting the computational fluid dynamics (CFD) code validation and theoretical model development by producing a high-quality experimental database of gas–liquid flow in a vertical pipe.

2. Experimental methodology

The present experimental campaign was carried out using an inclined closed pipe flow rig shown schematically in Fig. 2, that was reported previously by Abdulkadir et al. (2014a,b, 2015, 2018). The technical details can be found in the reported papers. However, for the sake of completeness, a short description of the experimental rig is presented here. The rig works

Table 1 – Properties of the fluids at 1 bar and at the operating temperature of 20 ± 0.5 °C.

Fluid	Density (kg/m^3)	Viscosity (kg/m s)	Surface tension (N/m)
Air	1.18	0.000018	
Silicone oil	900	0.00525	0.02

as follows: The experimental rig entails a main test pipe section constructed from see-through poly (methyl methacrylate) glass. The 6 m test pipe section has an internal diameter of 0.067 m. Mounted on a rigid steel frame was a test pipe section that may be rotated and allowed to be fixed between -5° to 90° as shown in Fig. 2. Silicone oil and air were used as the system fluids. The air is supplied from the laboratory main compressor which maintains 6 bar, however, a pressure regulation valve is used to regulate the air supply to 2 bar. The discharge is open to the atmosphere, so the outlet pressure is near 0 Psig. At the inlet, the pressure varies depending on the flow conditions, due to the pressure drop. As a result, the pressure gage located after and next to the gas rotameters ranges from 0.5 to 8.9 Psig. The rest of the pressure drop occurs across the valve that controls the flow.

The design of the inlet section was such that it allows the injected air to be well mixed and equally spread across the cross-section of the pipe. It was predetermined according to Abdulkadir et al. (2014b), that the mixing of the air and silicone oil phases took place in such a manner as to reduce flow instability. Flow stability was accomplished by using a built mixing unit (annular section), providing the maximum time for the two-phases to develop. The mixing section is made from polyvinyl chloride (PVC) pipe as shown in Fig. 2b. The silicone oil was fed into the mixing chamber from one side and then flows around a perforated cylinder via which the air was fed through a distributor with 100 holes, with each having a diameter of 3 mm, thus creating a more even circumferential mixing section.

The two parallel airflow rotameters as shown in the figure; were used to measure the flow rates. The gas and liquid superficial velocities deployed were 0.05–6.20 m/s and 0.05–0.52 m/s, respectively. The physical properties of the air–silicone oil system are presented in Table 1.

To measure the void fraction, liquid holdup, and pressure drop along the length of the pipe, a sequence of experiments was carried out in this study using WMS, ECT, and DP Cell, respectively. The data were obtained with a data acquisition frequency of 1000, 200 and 200 Hz for the WMS, ECT and DP Cell, respectively. In total, 143 runs were carried out and the results of these experiments are presented and discussed in Section 3. It is worth mentioning that the development length for establishing steady-state conditions of fully developed two-phase flow in a 67 mm diameter pipe according to Abdulkadir et al. (2015) is 4 m (60 diameters). It is against this background that the measuring stations were located at ECT-plane 1, ECT-plane 2, WMS, DP cell-tapping 1 and DP cell-tapping 2 at 4.4 (66 diameters), 4.489 (67 diameters), 4.92 (73 diameters), 4.5 (67 diameters) and 5.36 m (80 diameters), respectively. At these measuring stations, it is expected that steady-state conditions have been established and instabilities and transients will be disregarded.

2.1. *Advanced instrumentation*

2.1.1. *Electrical capacitance tomography (ECT)*

Fig. 3 Fig. 4 shows the ECT system used in this work. It was supplied by Process Tomography Limited. The name of the model is PTL-300 system and is made up of a data processing unit PC, DAM-200 data acquisition unit and a capacitance sensor. The PC works using the Windows XP operating system and in addition runs the twin-plane ECT software designed for the PTL-300 system and the ECT 32 programme. The ECT 32 programme permits one or two ECT sensor planes to be controlled either independently or simultaneously, the data are captured and can be played back at different frame rates. The measurement data can be revealed as permittivity images, normalized capacitances or a combination of both.

Multiple electrodes are arranged around the boundary of the zone to ease measurements all over the sensing zone. According to Wang et al. (1995) and Yang (1996), the sensor usually consists of 8 or 12 electrodes mounted round, peripherally around the sensing zone. In this work, the number of sensor consists of 8 electrodes. A vital necessity of the imaging system is that the measuring circuit should only measure the capacitance between the selected pair of electrodes and that it should be unaffected by the stray capacitance between the measuring electrodes and earth. Therefore, to satisfy these requirements a stray immune capacitance measuring circuit that was developed by Xie et al. (1992) which uses switched-capacitor charge transfer was adopted in this work.

(a) ECT Calibration procedure, reconstruction algorithm and data processing: The calibration for the ECT system involved filling the sensor with the low permittivity material (air has a relative permittivity value of 8.9×10^{-12}) and taking a complete set of measurements followed by filling the sensor with the high permittivity material (silicone oil with a relative permittivity value of 2.7) and taking a complete set of measurements. This sets the lower and upper limits for all subsequent measurements.

It can be observed from Eq. (4) that when the sensor is full of air, the silicone oil's volume fraction will be zero and when it is full of silicone oil the volume fraction will be one. When the sensor contains both air and silicone oil the volume fraction Cr_i is calculated by assuming it is a linear function between the lower and upper limits set during calibration. This method has been successfully applied to a number of engineering applications including fluidized bed rig (Wang et al., 1995; Azzi et al., 2010), gas/liquid flow in pipes (Azzopardi et al., 2010), gas–liquid flow in bends (Abdulkadir et al., 2011), slug flow in horizontal and vertical pipes (Abdulkadir et al., 2014b, 2016) and void fraction distribution (Abdulkadir et al., 2018).

When silicone oil is introduced into air within the sensing zone the capacitance measurements between electrode pairs will increase. The ECT system measures these capacitance changes and reconstructs a cross-sectional image from the capacitance data. The capacitance measurements were then converted to normalized capacitance data for image recon-

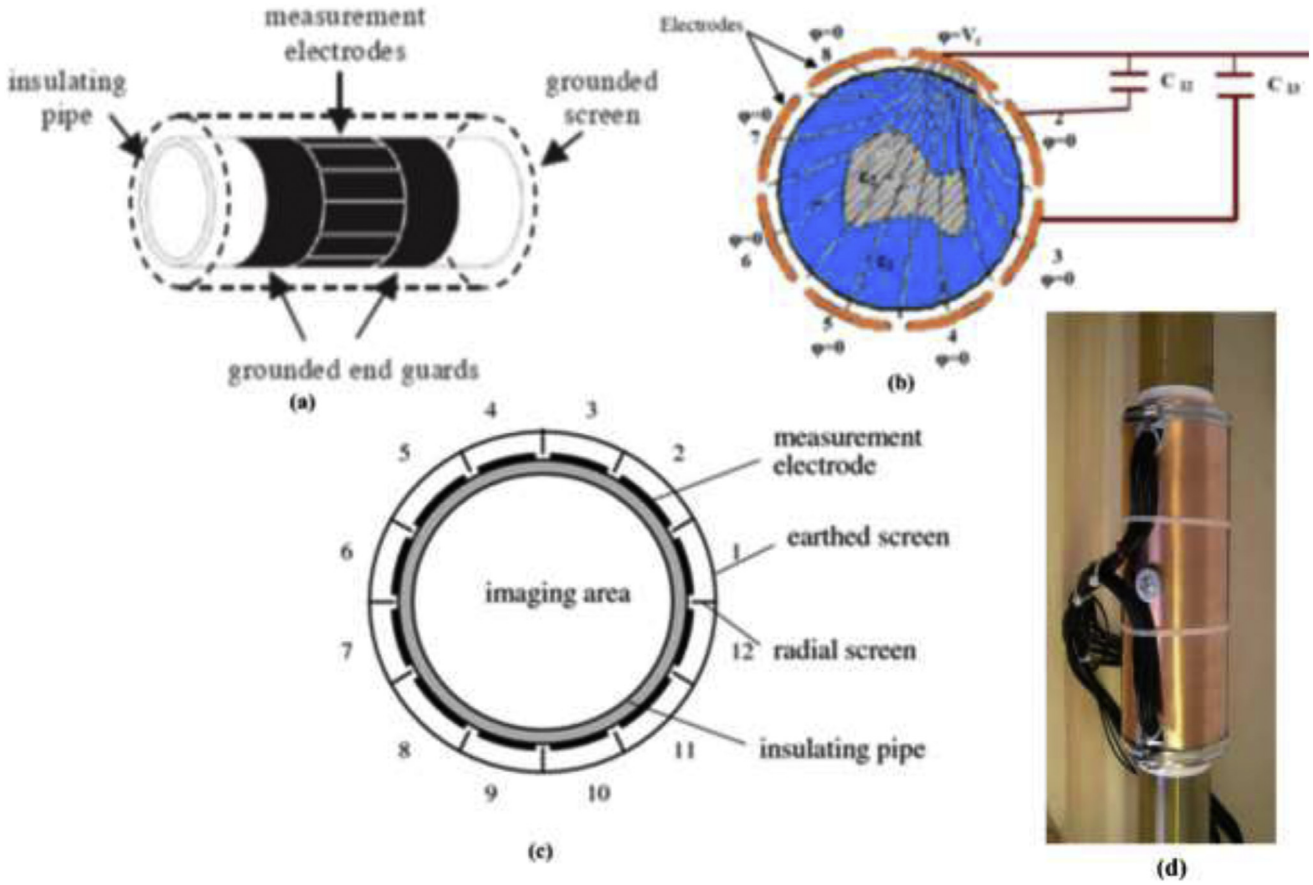

Fig. 3 – The electrical capacitance tomography (ECT) sensor (a) layout of driven guard electrodes; (b) an image reconstruction algorithm which translates the measurement data into the cross-sectional data into the cross-sectional concentration map; (c) layout of driven guard electrodes; (d) picture of the ECT.

struction based on a parallel capacitance model (Abdulkadir, 2011).

In order to represent the mathematical model for the process, it was assumed that:

(1) The capacitances when the whole sensor is completely filled with air and silicone oil are C_{oi} and C_{mi}, respectively.
(2) The capacitance plate area is unity.
(3) The mixture of air and silicone oil between the plates has a silicone oil fraction of Cr_i.
(4) That the dielectric distribution $\varepsilon(x, y)$ is independent of the sensitivity function S_i.

As, there are 28 independent capacitance measurements between any of the 8 electrodes in all likely combinations, the value of the ith capacitance C_i can be written based on Huang et al. (2003) as

$$C_i = \iint_D \varepsilon(x, y) S_i(x, y, \varepsilon(x, y)) dxdy, \quad i = 1, 2, \ldots, 28 \tag{1}$$

where D is the cross-sectional diameter of the pipe (image area).

In addition, since capacitance is proportional to capacitor plate area, the capacitance due to the silicone oil filled part of the sensor is $C_{mi}Cr_i$ and the capacitance due to the air filled part of the sensor is $C_{oi}(1 - Cr_i)$ (Bolton et al., 1998a). Since the air and silicone oil are in a parallel arrangement, thus the total parallel capacitance C_i is equal to the sum of these two capacitances, i.e.

$$\begin{aligned} C_i &= C_{mi}Cr_i + C_{oi}(1 - Cr_i) = C_{mi}Cr_i + C_{oi} - C_{oi}Cr_i \\ &= Cr_i(C_{mi} - C_{oi}) + C_{oi} \\ C_i - C_{oi} &= Cr_i(C_{mi} - C_{oi}) \end{aligned} \tag{2}$$

Rearranging this gives the normalized capacitance measurements Cr_i,

$$Cr_i = \frac{C_i - C_{oi}}{C_{mi} - C_{oi}}, \quad i = 1, 2, \ldots, 28 \tag{3}$$

As capacitance is proportional to material permittivity (Bolton et al., 1998a), permittivity was substituted for capacitance as follows:

$$Cr_i = \frac{\varepsilon_{mi} - \varepsilon_o}{\varepsilon_m - \varepsilon_o} \tag{4}$$

where C_{oi} is the ith measured capacitance when the pipe is filled with air. In this case, $\varepsilon(x, y) = \varepsilon_o$, and according to Eq. (1) $C_{oi} = \iint_D \varepsilon_o(x, y) S_i(x, y) dxdy$. C_{mi} is the value of the i_{th} capacitance when the pipe is completely filled with silicone oil. In this case, $\varepsilon(x, y) = \varepsilon_m$, and $C_{mi} = \iint_D \varepsilon_m(x, y) S_i(x, y) dxdy$. ε_0 is the dielectric constant (permittivity) of air. ε_m is the dielectric constant (permittivity) of silicone oil.

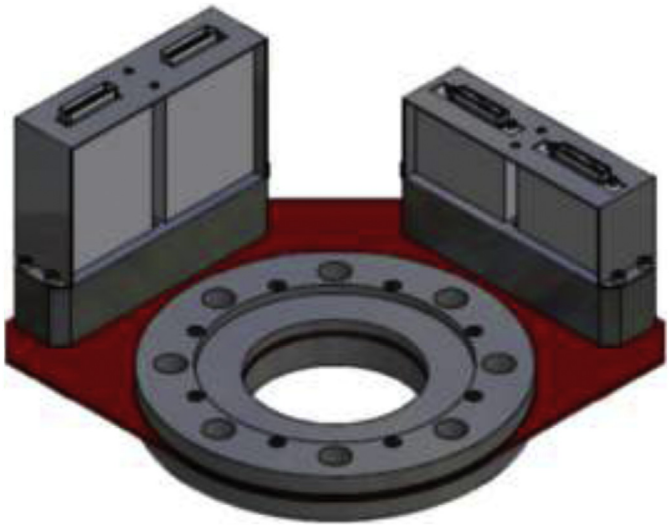

Fig. 4 – Wire mesh sensor (WMS) used during experimentation.

Thus, Eq. (3) according to Abdulkadir (2011) can be written as

$$Cr_i = \frac{\iint_D \varepsilon(x,y)S_i(x,y)dxdy - \iint_D \varepsilon_o S_i(x,y)dxdy}{\iint_D \varepsilon_m S_i(x,y)dxdy - \iint_D \varepsilon_o S_i(x,y)dxdy} \quad (5)$$

$$Cr_i = \frac{\iint_D \left(\frac{\varepsilon(x,y)-\varepsilon_o}{\varepsilon_m-\varepsilon_o}\right) S_i(x,y)dxdy}{\iint_D \left(\frac{\varepsilon_m-\varepsilon_o}{\varepsilon_m-\varepsilon_o}\right) S_i(x,y)dxdy} = \frac{\iint_D \left(\frac{\varepsilon(x,y)-\varepsilon_o}{\varepsilon_m-\varepsilon_o}\right) S_i(x,y)dxdy}{\iint_D S_i(x,y)dxdy} \quad (6)$$

2.1.2. *Wire mesh sensor (WMS)*

The WMS is well-known as a valuable research tool that can give significant amount of data, both spatially and temporally. The resolution of the sensor is superior to many other advanced instrumentations like the ECT. Conversely, this comes with accompanying shortcoming that the sensor is intrusive. The intrusiveness effect of WMS has been extensively investigated in the past, for instance Wangjiraniran et al. (2005); evaluated it against high-speed filming, Prasser et al. (2005) appraised it against a fast x-ray tomography system and Sharaf et al. (2016) assessed it against gamma-ray densitometry. The findings from their results showed that the sensor produces images of an undisturbed flow, uncertainty was found to be in the 10% range for void fraction measurement. Da Silva et al. (2011) concluded therefore that the WMS is an excellent tool to experimentally investigate two-phase gas–liquid flows.

It is worthy of mention that an associated electronic sensor measures the local permittivity in the gaps of all crossing points by successfully applying an excitation voltage (sine wave of 5 MHz) to each one of the sender electrodes at one wire plane whilst measuring in parallel the current flowing toward receiver electrodes at the other wire plane. The non-activated transmitter wires are grounded. This step guarantees that the electrical field distribution is concentrated along the activated wire and permits for a sampling of only a well-defined section within the pipe so that the measured currents are explicitly related to the corresponding crossing point. For the permittivity measurements, a sinusoidal alternating voltage is applied and a demodulation scheme is subsequently applied. After digitizing, the measured data are sent to a computer where they are processed and displayed. The method can generate up to 7,000 images per second. Details of the electronic circuits used may be found in Da Silva et al., 2010 Da Silva et al. (2010).

WMS calibration procedure, reconstruction algorithm and data processing: According to Da Silva et al. (2010), the output reading of a wire mesh sensor is in the form of a data matrix $V(i,j,k)$ representing the voltage measured at each (i,j) crossing point with $i \in (1,\ldots,0.24)$ and $j \in (1,\ldots,0.24)$ and at a given time step k. These voltage readings are proportional to the relative permittivity of two-phase mixture ε_m

$$V = b\ln(\varepsilon_m) + c \quad (7)$$

where b and c are constants that incorporate the specific parameters of the electronics. Reference measurements are required to determine the constants b and c of Eq. (7), which in turn allows for the calculation of mixture permittivity at every crossing point. First, the sensor measures the empty pipe, i.e., air ($\varepsilon_{r,G} = 1$), providing the reference data matrix $V^G(i,j)$, which is usually an average of the raw data over an appropriate temporal range to subdue noise. The procedure is then repeated with the entire cross-section covered with the liquid phase having a permittivity value $\varepsilon_{r,L}$, full pipe, which gives another reference data matrix denoted by $V^L(i,j)$. Finally, on the basis of Eq. (7) for the two described conditions, the measured mixture permittivity is calculated by

$$V(i,j,k) = b\ln\varepsilon_m(i,j,k) + c \quad (8)$$

subject to the boundary conditions:

$$\varepsilon_m(i,j,k) = \varepsilon_{r,G} = 1; \quad V(i,j,k) = V^G(i,j)$$

$$\varepsilon_m(i,j,k) = \varepsilon_{r,L}; \quad V(i,j,k) = V^L(i,j)$$

The values of the boundary conditions are then substituted into Eq. (8) and solving simultaneously to obtain the values of the constants, b and c as:

$$b = \frac{V^L(i,j) - V^G(i,j)}{\ln\varepsilon_{r,L}} \quad (9)$$

$$c = V^G(i,j) = b\ln 1 + c \quad (10)$$

Substituting Eqs. (9) and (10) into (8) to obtain $\varepsilon_m(i,j,k)$

$$\varepsilon_m(i,j,k) = \exp\left[\left(\frac{V(i,j,k) - V^G(i,j)}{V^L(i,j) - V^G(i,j)}\right)\ln\varepsilon_{r,L}\right] \quad (11)$$

The void fraction based on the parallel model is obtained from the measured permittivity ε_m according to

$$\alpha(i,j,k) = \frac{\varepsilon_{r,L} - \varepsilon_m(i,j,k)}{\varepsilon_{r,L} - \varepsilon_{r,G}} \quad (12)$$

where $\varepsilon_{r,L}$ is the liquid permittivity and $\varepsilon_{r,G}$(=1) is the gas permittivity.

Quantitative insights of the flow are obtained by averaging the measured void fraction in space and/or in time, yielding a time series of void fraction or mean void fraction over the entire measurement.

2.1.3. *Pressure drop measurement using a differential pressure transducer (DP cell)*

Fig. 5 shows a DP cell (Rosemount 1151 smart model) with a range of 0–37.4 kPa, output voltage of 1 to 5 volts and a data acquisition frequency of 200 Hz that was used to measure the

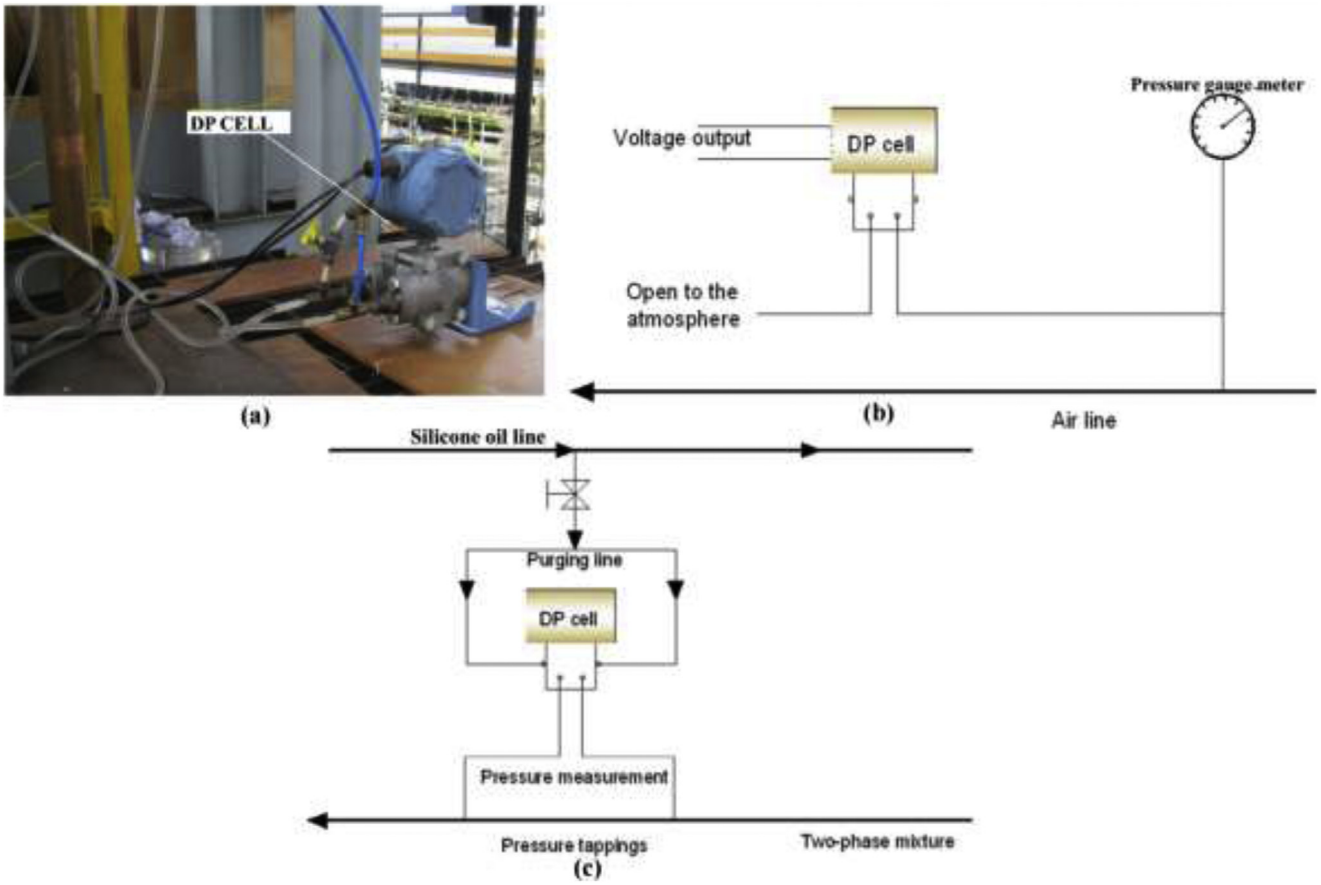

Fig. 5 – (a) An image of the DP cell arrangement; (b) a detailed arrangement for carrying out DP cell calibration and (c) a detailed DP cell purging arrangement.

pressure drop in this work. Both the sensitivity and range were taken into consideration in the selection of the DP cell. The DP cell was used to measure the time-varying two-phase total pressure drop across the test section. To achieve this, two pressure tapping were provided, located in the vertical pipe. The particular axial locations of the tappings are 4.5 and 5.36 m from the foot of the test section. Hence, the total pressure drop was measured concurrently with the void fraction and liquid holdup.

Before the commencement of making measurements of pressure drop, the DP cell had to be calibrated using the procedure shown in Fig. 5. The calibration exercise carried out established the link between the output voltage of the DP cell and the differential pressure. It can be observed from Fig. 6 that the calibration curve is linear.

It is worthy of mention that for accurate pressure drop measurements, the pressure tappings in gas-liquid flow need to be purged frequently. Otherwise, pressure fluctuations will introduce a two-phase mixture into the DP cell lines triggering incorrectness in the measured pressure drop as a consequence of surface tension effects and indefinite hydrostatic head. It was against this backdrop that a purging system was used to keep an uninterrupted liquid line (silicone oil) to the DP cell from the pressure tappings.

Purging was carried out before the commencement of each run via opening and closing of the valve from the liquid line. The separation distance between the tappings was 86 cm. In order to activate the purging system, a high purging rate was fixed to liberate any available bubbles in the purging lines. An optimum purging rate which was suggested by Holt (1996) to be <5% of the total liquid flow rate was used.

2.2. *Empirical void fraction correlations*

In this work, 10 void fraction empirical correlations available in the literature were chosen for evaluation. They are shown in Table 2 in chronological order. The selection of the correlations considered factors such as pipe characteristics, flow orientation, pipe inclination and the fluids involved. Statistical analysis of the performance of the empirical correlations was carried out to find the best for the void fraction prediction. Eqs. (13)–(23) were used to calculate values of average void fraction and the obtained values are presented in Table 3.

3. Results and discussion

The gas and liquid superficial velocities deployed in this work are 0.05–6.2 and 0.05–0.52 m/s, respectively. The ensuing flow patterns detailed for liquid and gas superficial velocities of 0.05–0.52 and 0.05–0.288, 0.05–0.52 m/s and 0.34–0.95 and 0.05–0.52 and 1.42–6.2 m/s are spherical cap bubble, slug, and churn flows, respectively.

3.1. *Flow pattern map under current experimental conditions*

Fig. 7 shows the flow pattern map for the present experimental campaign concerning vertical gas–liquid flow. The transition lines as depicted in the figure were obtained using the mechanistic models recommended by Taitel et al. (1980);

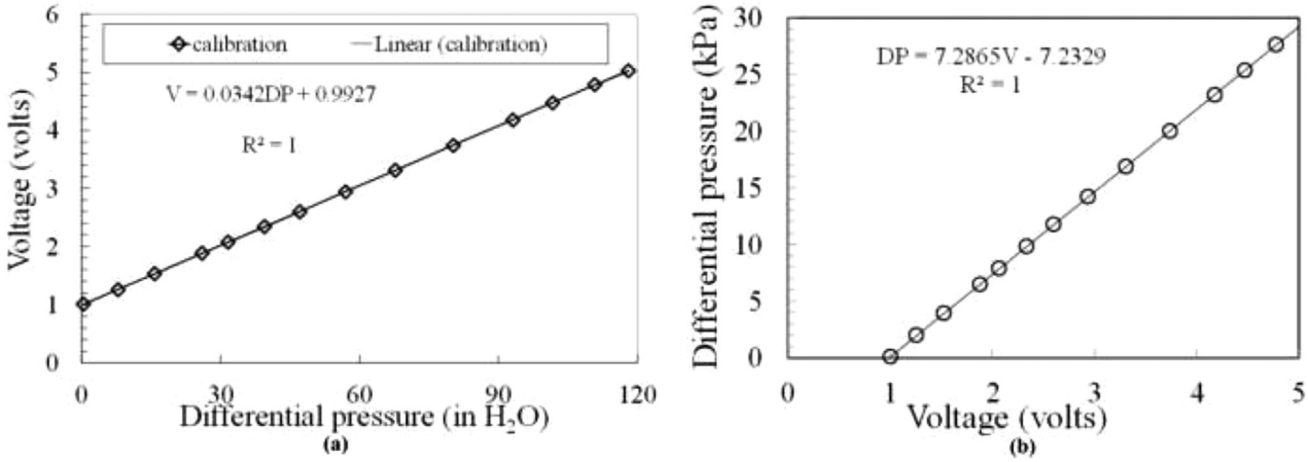

Fig. 6 – A detailed plot of DP cell calibration curve.

Table 2 – The list of 10 selected empirical correlations.

Serial number	Empirical model	Model equation	System	Equation
1	Hughmark (1962)	$\varepsilon = 0.82\left(\frac{U_{SG}}{U_{SG}+U_{SL}}\right)$	Mercury–nitrogen	(13)
2	Nicklin et al. (1962)	$\varepsilon = \frac{U_{SG}}{1.2U_M+0.35\sqrt{gD}}$	Air–water	(14)
3	Neal and Bankoff (1965)	$\varepsilon = 1.25\left(\frac{U_{SG}}{U_M}\right)^{1.88}\left(\frac{U_{SL}^2}{gD}\right)^{0.2}$	Mercury–nitrogen	(15)
4	Greskovich and Cooper (1975)	$\varepsilon = \frac{U_{SG}}{1.0U_M+0.671\sqrt{gD(\sin\theta)^{0.263}}}$	Air–water	(16)
5	Jowitt et al. (1984)	$\varepsilon = \frac{U_{SG}}{\left(\left[1+0.796EXP\left(-0.061\sqrt{\frac{\rho_L}{\rho_G}}\right)\right]U_M+0.034\left(\sqrt{\frac{\rho_L}{\rho_G}}-1\right)\right)}$	Rod bundle	(17)
6	Clark and Flemmer (1985)	$\varepsilon = \frac{U_{SG}}{1.07U_M+1.53\left(g\sigma\left(\frac{\rho_L-\rho_G}{\rho_L^2}\right)\right)^{0.25}}$	Air–water	(18)
7	Hasan and Kabir (2010)	$\varepsilon = \frac{U_{SG}}{1.2U_M+V_s}$ $\quad V_s = 0.35\left[\frac{gD(\rho_L-\rho_G)}{\rho_L}\right]^{0.5}$	Air–water	(19) (20)
8	Kokal and Stanislav (1989)	$\varepsilon = \frac{U_{SG}}{1.2U_M+0.345\sqrt{gD\left(1-\frac{\rho_G}{\rho_L}\right)}}$	Air–oil	(21)
9	Coddington and Macian (2002)	$\varepsilon = \frac{U_{SG}}{1.08U_M+0.45}$	Air–water	(22)
10	Hasan (1995 Hassan (	$\varepsilon = \frac{U_{SG}}{1.12U_M+0.345\sqrt{gD\left(1-\frac{\rho_G}{\rho_L}\right)}}$	Air–water; Air–oil; Air–lube oil	(23)

Table 3 – Performance of empirical models based on flow pattern: spherical cap bubble.

	Spherical cap bubble flow			
	ε	MSE	RMSE	MAPE (%)
Base case	0.106			
Nicklin et al. (1962)	0.362	0.06693	0.256	241.51
Neal and Bankoff (1965)	0.125	0.0007780	0.019	17.92
Greskovich and Cooper (1975)	0.125	0.004340	0.007	6.604
Jowitt et al. (1984)	0.126	0.001234	0.025	23.58
Hasan and Kabir (2010)	0.169	0.0007798	0.055	51.89
Clark and Flemmer (1985)	0.126	0.0008214	0.057	53.77
Hasan and Kabir (2010)	0.0807	0.0009542	0.019	17.92
Kokal and Stanislav (1989)	0.0995	0.0001911	0.02	18.87
Coddington and Macian (2002)	0.092	0.0007435	0.014	13.21
Hasan (1995)	0.0515	0.003661	0.023	21.70

model for bubbly/slug transition, the Jayanti and Hewitt (1992) slug/churn transition model and the Pereyra and Torres (2005) model. It can be observed from the figure that the Pereyra and Torres (2005) model predicts spherical bubble as bubble flow. Also, the Jayanti and Hewitt slug-churn flow transition line is at the far right side of the map for all the gas and liquid superficial velocities considered. It implies, therefore, that only the slug flow but no churn flow is predicted by the map. Also embedded in the flow pattern map is a schematic representation of the flow patterns and 2-dimensional slice views of the void fraction seen for different liquid and gas superficial velocities. It is established that these observations corroborate the results presented on the map. At low gas superficial velocities of 0.05 to 0.29 m/s, bubbles of large size can be seen even though not as large as the pipe diameter. These bubbles are referred to as spherical cap bubbles based on the description of Costigan and Whalley (1997). With an increase in gas superficial velocity to 0.34–0.70 m/s, the merging of these spherical

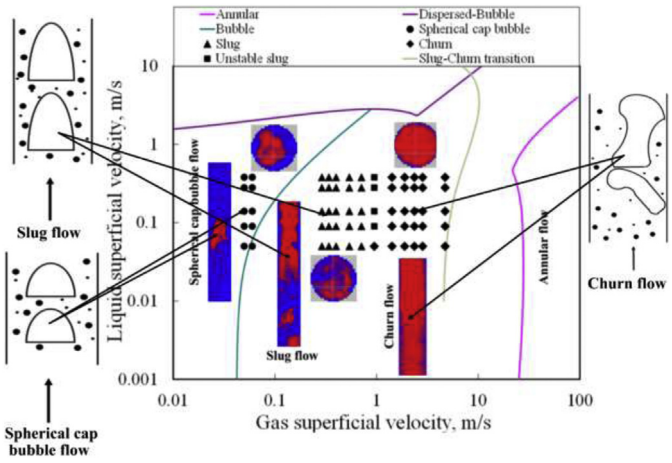

Fig. 7 – Flow pattern map under current experimental conditions predicted by Pereyra and Torres (2005) and reconstructed images of the air–silicone oil flow evolution from spherical cap bubble to churn flow.

cap bubbles promotes the formation of slug flow. When the gas superficial velocity is between 1.2 – 6.2 m/s, the unstable slug flow is seen to transform to churn flow. These observations can be seen to be in good agreement with the flow pattern map shown on the same plot, Fig. 7.

3.2. *Comparison between present study and that of Hernandez-Perez (2008)*

A comparison between the present study and that of Hernandez-Perez (2008) will be made based on the void fraction. Hernandez-Perez (2008), carried out experimental work on a vertical 67 mm internal diameter pipe and the fluids employed were air and water. He deployed conductance WMS to obtain void fraction.

The results of the comparison presented in Fig. 8 are carried out at the same liquid superficial velocity of 0.2 m/s and gas superficial velocity of 0.28–3.6 m/s. The plot shows the same tendency, though the values of void fraction from the work of Hernandez-Perez (2008) air-water published data at

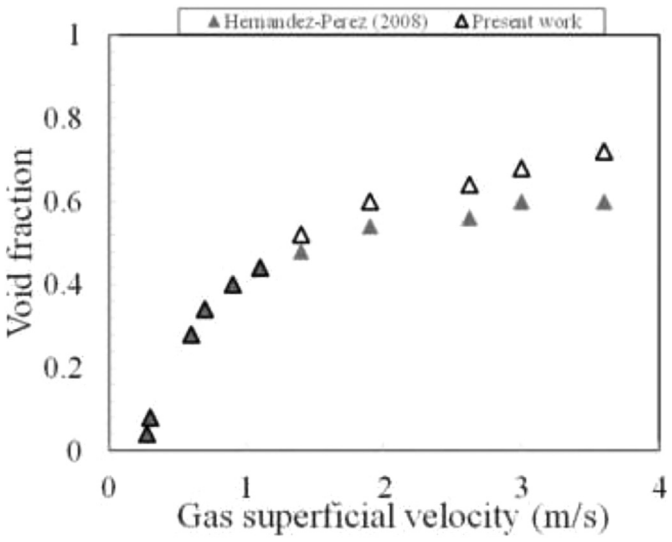

Fig. 8 – Comparison between present void fraction data for air–silicone oil against air–water experimental data of Hernandez-Perez (2008) at liquid superficial velocity of 0.2 m/s and gas superficial velocity of 0.28–3.6 m/s.

higher gas superficial velocities of 1.4 to 3.6 m/s are higher than those of present study. This behaviour can be attributed to the effect of fluid properties. At lower gas superficial velocities of 0.28 to 1.1 m/s, the Hernandez-Perez data and present data depict the same values. This implies that at these gas superficial velocities, the fluid properties do not affect void fraction.

3.3. *Comparison of time series and PDFs of void fraction for the WMS, ECT and DP cell for the vertical pipe*

The PDFs of void fractions has been used to categorize the flow patterns in the same way as Abdulkadir et al. (2014a,b, 2015) and Prasser et al. (2005). A PDF according to Abdulkadir et al. (2014a) can be defined as the variation of the probability that the void fraction values lie within a certain range ($\varepsilon + \delta\varepsilon$) versus void fraction. It was determined by counting the number of data points in data bins of width 0.01 centred on void fractions from 0.005, 0.015, . . ., 0.995, and then dividing each sum by the total number of data points. They confirm the dominant void fractions which are observed for each flow condition.

Fig. 9 presents a comparison between the PDFs of void fraction for the ECT, WMS and DP cell for the same liquid and gas superficial velocities in a vertical pipe. It is worth mentioning that the time-averaged pressure drop was converted into a normalized probability density function (PDF). The relative frequency count data of the normalized pressure drop data was then calculated using the bin size of 0.02. Then the relative frequency data was fitted with normalized Gaussian to obtain PDF plots. Thus, the normalized pressure drop is approximately equal to the void fraction in the measurement section.

A single peak at low void fraction complemented by a widening tail, the signature of spherical cap bubble as described by Abdulkadir et al. (2014a,b, 2015) and Costigan and Whalley, 1997 Costigan and Whalley (1997) can be seen from the ECT and WMS measurements, Fig. 9(a-b). Thus, the results show that both instruments predict similar flow pattern signatures. On the contrary, a single peak can be seen at a low void fraction from the DP cell measurement. This according to Costigan and Whalley, 1997 Costigan and Whalley (1997) characterises bubble flow.

The PDF of void fraction as observed from the WMS and ECT data shown in Fig. 9(c-d) displays a double peak feature with one at a higher void fraction whilst the other at a lower void fraction. This denotes slug flow according to Abdulkadir et al. (2014a,b, 2015) and Costigan and Whalley, 1997 Costigan and Whalley (1997). The DP cell data conversely depicts the features of unstable slug flow with a mean peak at a void fraction of 0.65, but with two tails down to 0.38 and 0.96. The observed difference between the results from the 3 measuring instruments can be attributed to the fact that the measurements are averaged over a different length for each case. For the ECT, the measurements are averaged over a section of 0.089 m, which is the length of the electrodes. For the WMS, the measurements are more localised, as they are taken over the separation between the two planes of wires, which is 0.003 m. For the DP cell, the distance is much bigger, 0.86 m, therefore more averaged.

The PDF graphs of void fraction from the ECT, WMS and DP cell data shown in Fig. 9(e-f) displays the characteristic features of churn flow according to Abdulkadir et al. (2014a,b, 2015) and Costigan and Whalley, 1997 Costigan and Whalley (1997); a single peak at a high void fraction accompanied

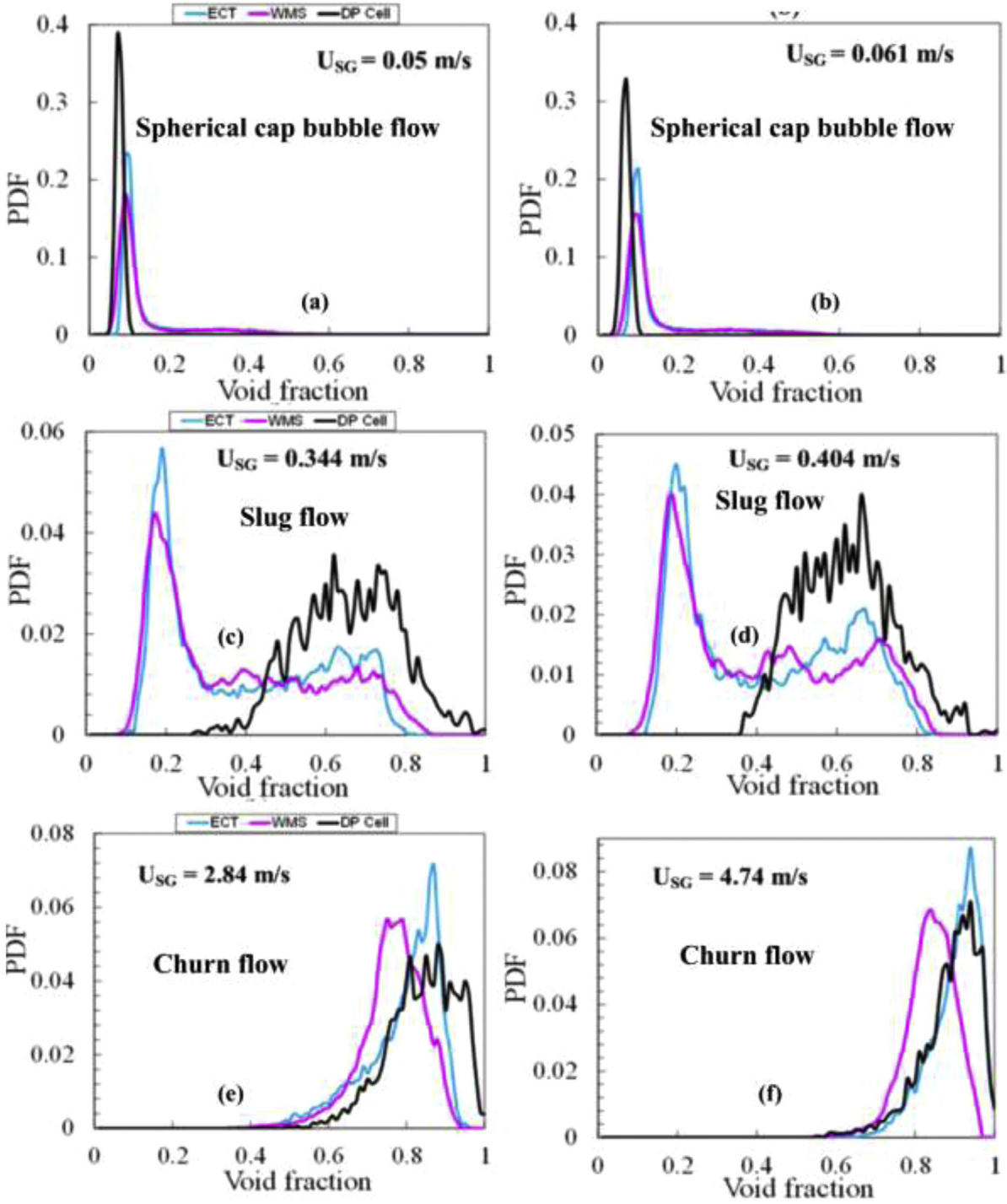

Fig. 9 – PDF of void fraction and dimensionless pressure gradient for (a,b) spherical cap bubble flow, (c,d) slug flow and (e,f) churn flow at liquid superficial velocity of 0.05 m/s and various gas superficial velocities of 0.05 to 4.74 m/s.

by a widening end down to a lower void fraction. The result depicts that the three measuring instruments predict similar flow regime signatures.

3.4. *Total, gravitational and frictional pressure gradients*

The DP transducer placed in between the twin-plane ECT was used to measure the total pressure gradient while the frictional pressure gradient, on the other hand, was achieved by deducting the hydrostatic (gravitational) term from the experimentally determined total pressure gradient. The distance between the pressure tappings is 0.86 m. The total pressure gradient was determined by dividing the measured pressure drop by 0.86 m, the gravitational pressure and frictional pressure gradients were then deduced (as described earlier in the text). Fig. 10(a-c) shows a plot of the effect of the variation of gas superficial velocity on total, gravitational and frictional pressure gradients with liquid superficial velocity as a parameter.

Fig. 10(a) shows that the total pressure gradient drops with a rise in gas superficial velocity for a given liquid superficial velocity. This decrease can be attributed to the fact that the flow is gravity dominated as also depicted in Fig. 10(b), and that a rise in gas superficial velocity provokes growth in void fraction, thus, reduces the two-phase mixture density. Also,

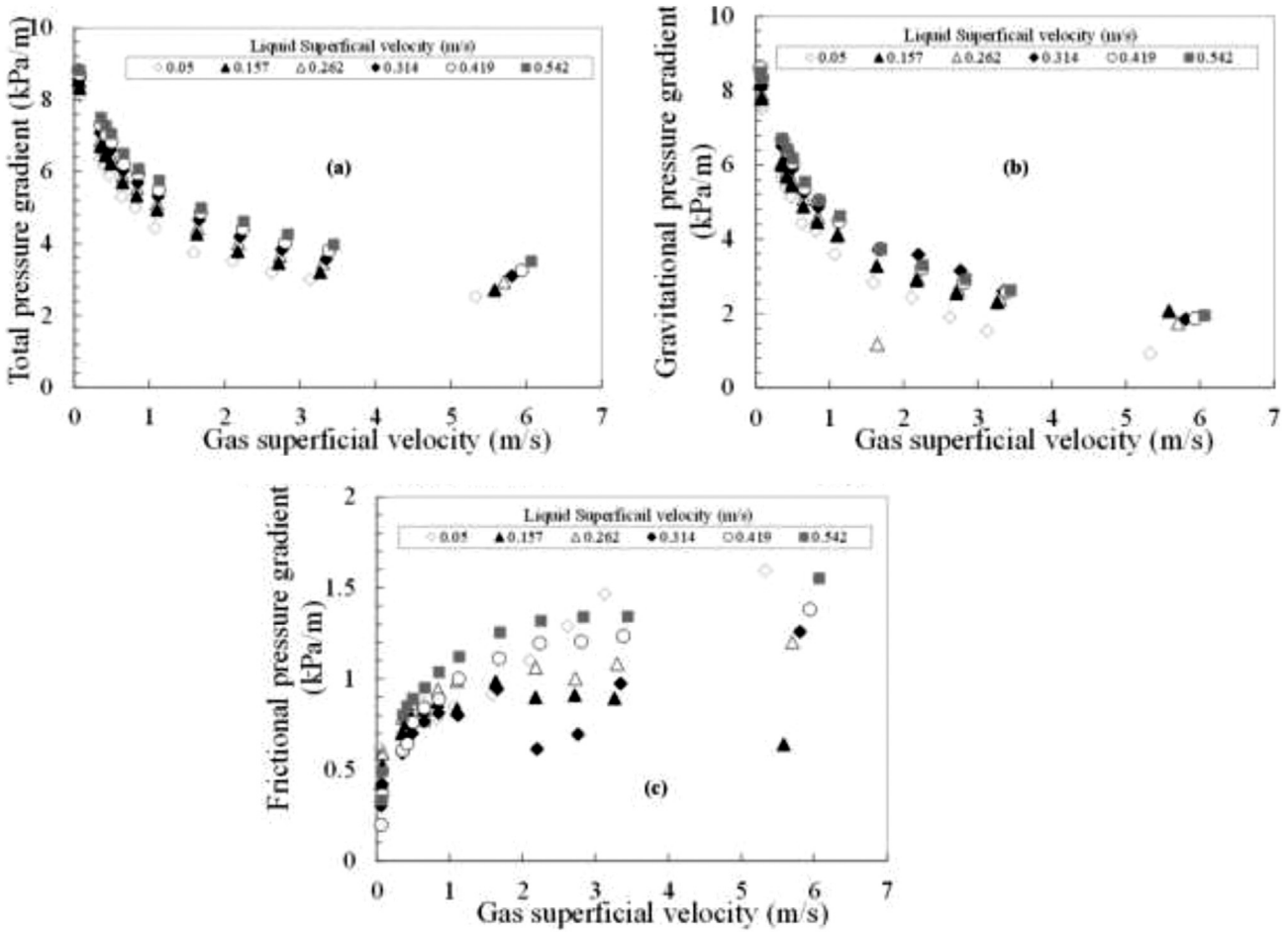

Fig. 10 – Variation of gas superficial velocity on (a) total pressure gradient, (b) gravitational pressure gradient and (c) frictional pressure gradient with liquid superficial velocity as a parameter.

the velocities met are not sufficient, to provoke high frictional pressure gradient and as such a rise in gas superficial velocity will bring about a consistent decrease in total pressure gradient.

Conversely, the frictional pressure gradient generally rises with an increase in the gas superficial velocity. According to Abdulkadir et al., 2014b Abdulkadir et al. (2014b), the rise in frictional pressure gradient can be associated with the fact that an increase in gas superficial velocity provokes higher assembly of gas bubbles, which progressively raises the true liquid velocity due to an increase in void fraction.

Comparison of average void fraction from experimental data (base case) and selected empirical correlations with consideration for flow patterns.

The experimental data is sorted at first here according to the prevailing flow patterns into spherical cap bubble, slug and churn flow. The performance of the ten selected empirical correlations is then tested against experimental data using statistical analysis, mean square error (MSE), root mean square error (RMSE) and mean absolute percentage error (MAPE), to select the candidate correlation. The mean square error (MSE), root mean square error (RMSE) and mean absolute percentage error (MAPE) are defined mathematically as:

$$MSE = \frac{1}{N}\sum_{i=1}^{N}\left(\varepsilon_{measured} - \varepsilon_{predicted}\right)^2 \tag{24}$$

$$RMSE = \sqrt{\frac{\sum_{i=1}^{N}\left(\varepsilon_{measured} - \varepsilon_{predicted}\right)^2}{N}} \tag{25}$$

$$MAPE = \frac{\sum_{i=1}^{N}\left|\frac{\varepsilon_{measured}-\varepsilon_{predicted}}{\varepsilon_{measured}}\right|}{N} \times 100\% \tag{26}$$

where N is the number of experimental data points.

Eqs. (24)–(26) were used to determine the MSE, RMSE and MAPE, respectively and the obtained values are presented in Tables 3–5.

Fig. 11(a) presents a cross plot of the experimental (base case) average void fraction against the predicted values from the ten selected empirical correlations, with emphasis on flow pattern dependency. On the other hand, Fig. 11(b) presents a cross plot of the experimental (base case) average pressure gradient band against the predicted values from the ten selected empirical correlations.

For the spherical cap bubble flow regime as depicted in Table 3, the Hughmark (1962) correlation show the largest MSE, RMSE and MAPE values of 0.06693, 0.256 and 241.51%, respectively. On the other hand, Neal and Bankoff (1965) correlation show the smallest RMSE and MAPE values of 0.007 and 6.607%, respectively. It is worthy of mention that the Kokal and Stanislav, 1989 Kokal and Stanislav (1989) correlation show the smallest MSE value of 0.0001911.

Table 4 – Performance of empirical models based on flow pattern: slug flow.

	Slug flow			
	ε	MSE	RMSE	MAPE (%)
Base case	0.425			
Nicklin et al. (1962)	0.709	0.08272	0.284	66.82
Neal and Bankoff (1965)	0.503	0.006257	0.078	18.35
Greskovich and Cooper (1975)	0.503	0.03518	0.071	16.71
Jowitt et al. (1984)	0.505	0.0007907	0.013	3.05
Hasan and Kabir (2010)	0.612	0.006272	0.11	25.88
Clark and Flemmer (1985)	0.530	0.006608	0.147	34.59
Hasan and Kabir (2010)	0.438	0.01126	0.078	18.35
Kokal and Stanislav (1989)	0.354	0.008923	0.08	18.82
Coddington and Macian (2002)	0.457	0.001415	0.032	7.53
Hasan (1995)	0.315	0.01266	0.105	24.71

Table 5 – Performance of empirical models based on flow pattern: Churn flow.

	Churn			
	ε	MSE	RMSE	MAPE (%)
Base case	0.734			
Nicklin et al. (1962)	0.793	0.01019	0.059	8.04
Neal and Bankoff (1965)	0.728	0.00469	0.006	0.817
Greskovich and Cooper (1975)	0.728	0.01563	0.295	40.19
Jowitt et al. (1984)	0.729	0.00664	0.045	6.131
Hasan and Kabir (2010)	0.838	0.00469	0.108	14.714
Clark and Flemmer (1985)	0.776	0.1680	0.037	5.04
Hasan and Kabir (2010)	0.779	0.00633	0.006	0.817
Kokal and Stanislav (1989)	0.439	0.09673	0.005	0.68
Coddington and Macian (2002)	0.755	0.1789	0.021	2.86
Hasan (1995)	0.626	0.01620	0.042	5.72

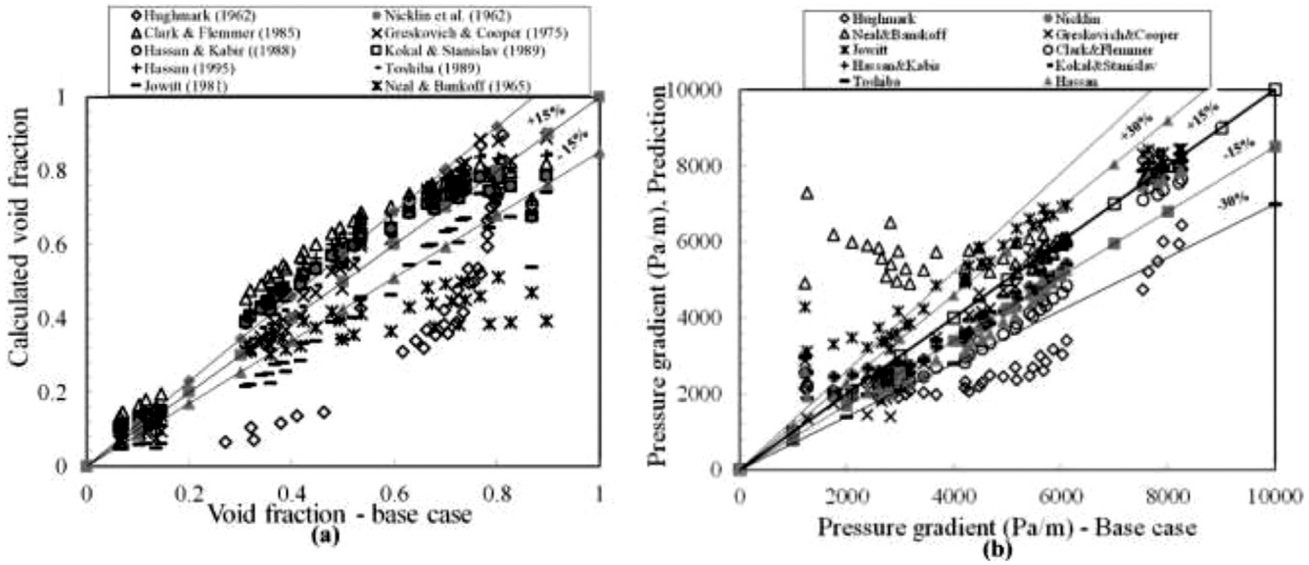

Fig. 11 – (a) Comparison between experimental average void fraction against predicted values with no flow pattern consideration using ±15% error limit. (b) Comparison between experimental pressure gradient against predicted values with no flow pattern consideration using ±15% and ±30%) error limits.

On the matter of slug flow, as shown in Table 4, the Greskovich and Cooper, 1975 Greskovich and Cooper (1975) correlation shows the smallest MSE, RMSE and MAPE values of 0.0007908, 0.013 and 3.05%, respectively. For the highest values, the Hughmark (1962) correlation shows MSE, RMSE and MAPE values of 0.08272, 0.284 and 66.82%, respectively.

According to Table 5 on the matter of churn flow, the Kokal and Stanislav (1989) correlation show the smallest RMSE and MAPE values of 0.005 and 0.68%, respectively. From the table, the Jowitt et al. (1984) and Nicklin et al. (1962) correlations show the smallest MSE value of 0.000469. On the other hand, the highest values for the RMSE and MAPE are 0.295 and 40.19%, respectively, for the Neal and Bankoff (1965) correlation. Interestingly, the Coddington and Macian (2002) correlation depict the highest MSE value of 0.1789.

Here, criteria that the average predicted void fraction is within with a 30% spread are used to consider the predictive performance of a correlation as satisfactory. Therefore,

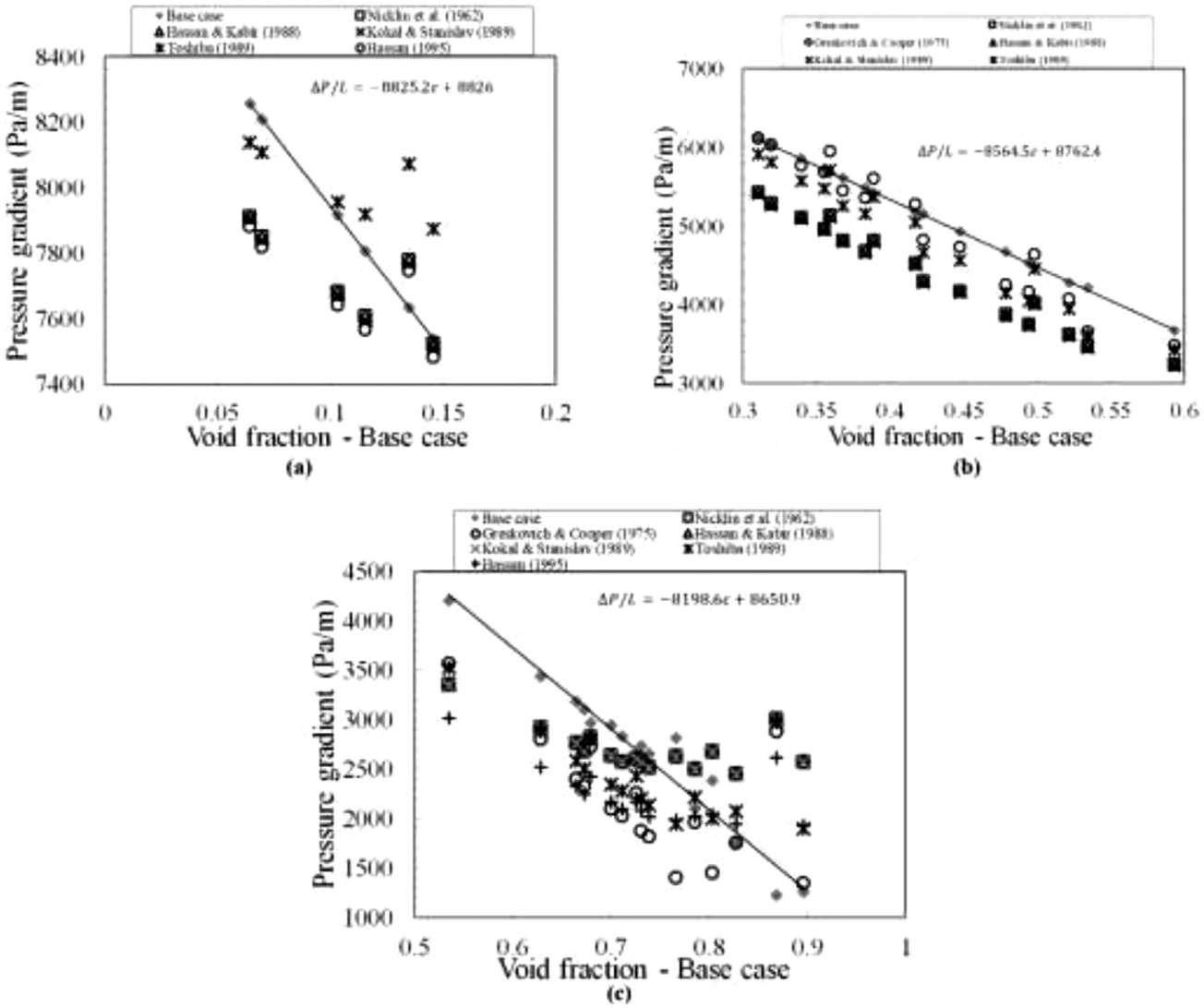

Fig. 12 – Prediction of pressure gradient for (a) bubble flow, (b) slug flow and (c) churn flow.

at a void fraction less than 0.2 as shown in Fig. 11(a), Neal and Bankoff (1965) correlation falls within the acceptable limit but completely falls outside the -15% width as the void fraction increases above 0.4. This is because the model does not account for drift velocity. Kokal and Stanislav (1989) correlation, on the other hand, gives excellent prediction at higher values of void fraction greater than 0.5, indicating its good performance for gas-dominated flows. However, the Coddington and Macian (2002) correlation give values of void fraction within +15% band for all void fraction above 0.3. Greskovich and Cooper (1975) correlation continued to show excellent prediction within the +15% limit.

From Fig. 11(b), the Greskovich and Cooper (1975) correlation gives the best match for the range of 4000 to 6000 Pa/m but under-estimates at lower pressure gradient values. Since the pressure gradient profile of two-phase systems declines with increasing void fraction, it implies that Greskovich and Cooper (1975) correlation performs better in a low gas dominated flow. Also from Fig. 11(b), it can be seen that the Greskovich and Cooper (1975) correlation slightly over-predicts higher pressure gradients. It can, therefore, be concluded that the Greskovich and Cooper (1975) correlation gives the best performance for the slug flow regime. Hasan (1995) correlation, on the other hand, continues to show the tendency for under-predicting pressure gradient but gives an excellent match at the higher pressure gradients between 7500 to 8500 Pa/m. Furthermore, Nicklin et al., 1962 Nicklin et al. (1962) correlation gives a good agreement from 2000 to 4000 Pa/m then under-predicts and again gives a good prediction at much higher pressure gradient from 7500 Pa/m and above. This tendency from the Nicklin et al., 1962 Nicklin et al. (1962) correlation can be attributed to the presence of drift flux velocity term in the model equation which depends solely on the pipe diameter without considering the fluid characteristics. This is why the performance of the model remains fairly constant and is not sensitive to flow pattern variations.

3.5. *Prediction of pressure gradient for bubble, slug and churn flows*

All the curves in Fig. 12 show that the pressure gradient decline as the void fraction increases. This behaviour is expected as the system under study is a vertical pipe; the primary contributor to the overall pressure gradient is the gravitational pressure which depends on the density of the fluids. Since air (the gas phase in this study) is lighter than silicone oil (the liquid phase in this study), as expected, the hydrostatic head will decline with increasing gas superficial velocity. Nicklin et al., 1962 Nicklin et al. (1962), Hasan and Kabir (2010), Kokal and Stanislav (1989) and Hasan, 1995 Hasan (1995) empirical cor-

relations all under-predict the pressure gradient for all three flow patterns being considered. However, the Coddington and Macian (2002) correlation intersects the base case pressure gradient at about 8000 Pa/m and progressively over-predict the pressure gradient as the void fraction increases.

Fig. 12(b) shows that the slope of the decline is 8564 Pa/m, which is less than the observed slope in Fig. 12(a), 8825 Pa/m. This reduction in pressure gradient is expected as the two-phase flow moves from a predominantly liquid dominated flow (bubble) to flow with an increased gas population (slug flow). All the considered empirical correlations performed fairly well in the slug flow regime as they all show nearly the same tendency in the pressure decline (the curves approximate parallel lines). But Greskovich and Cooper (1975) correlation give the best match to the pressure gradient base case.

It is worth mentioning that there is a further decline in the slope of pressure gradient graph (slope = 8198 Pa/m) with an increase in void fraction as shown in Fig. 12(c). This is because gas population increases rapidly with the expense of the liquid phase, and this leads to a reduction in the pressure gradient. It can be seen from the figure that the plots do not give perfect straight lines as in Figs. 12(a-b). The deviation from a straight-line relation suggests a consideration of the onset of significant friction forces with increased gas superficial velocity. The clustering of the points without a well-defined pattern shows the presence of uncertainties and instabilities, which indicates the presence of churn flow. Regarding the distribution of the points around the base case, it can be inferred that the Nicklin et al. (1962) correlation seems suitable for the pressure gradient prediction.

4. Conclusion

Experimental characterisation of two-phase air–silicone oil flow in a vertical 67 mm internal diameter pipe was successfully carried out by using a differential pressure transducer and advanced instrumentation such as electrical capacitance tomography (ECT) and wire mesh sensor tomography (WMS). The investigation was focused on the behaviours of pressure drop, void fraction and flow pattern in a range of gas superficial velocities from 0.05 to 6.2 m/s and liquid superficial velocities from 0.05 to 0.52 m/s. To the best of the authors' knowledge, no similar experimental work has been reported in the open literature, even though the operating conditions might be typically encountered in industrial applications, in particular, hydrocarbon transportation. Following conclusions can be drawn: The observed flow patterns from the present work are the spherical cap bubble, slug and churn flow. The slug-churn flow transition line is at the far right side of the map. It implies that only the slug flow but no churn flow is predicted by the map. The void fraction values from Hernandez-Perez (2008) for the air–water system at the gas superficial velocities of 1.4 to 3.6 m/s are higher than those in the present study. At the gas superficial velocities of 0.28 to 1.1 m/s, the values of void fraction from the two works agree well. The PDFs from the output of the DP cell for spherical cap bubble and slug flow regimes were significantly different from those obtained from the ECT and WMS. The PDFs of void fraction obtained from the outputs of the WMS, ECT and DP cell can be used to predict churn flow with confidence. The total and gravitational pressure gradients decrease with an increase in gas superficial velocity while, in contrast, the frictional pressure gradient increases with an increase in the gas superficial velocity. Neal and Bankoff, 1965 Neal and Bankoff (1965) correlation gave the best match for the void fraction in spherical cap bubble flow. The prediction from this correlation shows an average RMSE of about 6.6%. Greskovich and Cooper (1975) correlation showed the best prediction for the average void fraction in slug flow regime with the least MSE, RMSE and MAPE values of 0.0007908, 0.013 and 3.05%, respectively. Also within the slug flow regime, the Coddington and Macian (2002) correlation gave a very good fit for pressure gradient prediction with MAPE value of 13.85% when compared to the pressure gradient obtained from experiments. Kokal and Stanislav (1989) correlation showed progressively higher accuracy and stability with the increase of gas rates in RMSE and MAPE values of 0.005 and 0.68%, respectively, in the churn flow regime. Hence, it is a good correlation for transitional flow region.

Conflict of interest

None declared.

Acknowledgment

Abdulkadir, M., would like to express his sincere appreciation to the Nigerian government through the Petroleum Technology Development Fund (PTDF)for providing the funding for his doctoral studies.

This work has been carried out within the Joint Project on Transient Multiphase Flows and Flow Assurance. The Author(s) wish to recognize the contributions made to this project by the UK Engineering and Physical Sciences Research Council (EPSRC) and the following: GL Industrial Services; BP Exploration; CD-adapco; Chevron; ConocoPhillips; ENI; ExxonMobil; FEESA; IFP; Institutt for Energiteknikk; PDVSA (INTEVEP); Petrobras; PETRONAS; SPT; Shell; SINTEF; Statoil and TOTAL. The Author(s) wish to express their sincere gratitude for this support.

References

Abdulkadir, M., 2011. Experimental and Computational Fluid Dynamics (CFD) Studies of Gas–Liquid Flow in Bends (Ph.D. thesis). University of Nottingham, UK.

Abdulkadir, M., Zhao, D., Sharaf, S., Abdulkareem, L.A., Lowndes, I.S., Azzopardi, B.J., 2011. Interrogating the effect of 90° bends on air–silicone oil flows using advanced instrumentation. Chem. Eng. Sci. 66, 2453–2467.

Abdulkadir, M., Hernandez-Perez, V., Lowndes, I.S., Azzopardi, B.J., Brantson, E.T., 2014a. Detailed analysis of phase distributions in a vertical riser using wire mesh sensor (WMS). Exp. Therm. Fluid Sci. 59, 32–42.

Abdulkadir, M., Hernandez-Perez, V., Lowndes, I.S., Azzopardi, B.J., Dzomeku, S., 2014b. Experimental study of the hydrodynamic behaviour of slug flow in a vertical riser. Chem. Eng. Sci. 106, 60–75.

Abdulkadir, M., Hernandez-Perez, V., Lowndes, I.S., Azzopardi, B.J., 2015. Comparison of experimental and computational fluid dynamics (CFD) studies of slug flow in a vertical riser. Exp. Therm. Fluid Sci. 68, 468–483.

Abdulkadir, M., Hernandez-Perez, V., Lowndes, I.S., Azzopardi, B.J., Sam–Mbomah, E., 2016. Experimental study of the hydrodynamic behaviour of slug flow in a horizontal pipe. Chem. Eng. Sci. 156, 147–161.

Abdulkadir, M., Hernandez-Perez, V., Kwatia, C.A., Azzopardi, B.J., 2018. Interrogating flow development and phase distribution in vertical and horizontal pipes using advanced instrumentation. Chem. Eng. Sci. 186, 152–167.

Abdulkadir, M., Mbalisigwe, U.P., Zhao, D., Hernandez-Perez, V., Azzopardi, B.J., Tahir, S., 2019. Characteristics of churn and annular flows in a large diameter vertical riser. Int. J. Multiphase Flow 113, 250–263.
Ali, S.F., 2009. Two-Phase Flow in Large Diameter Vertical Riser (Ph.D. thesis). Cranfield University.
Azzi, A., Azzopardi, B.J., Abdulkareem, L.A., Hilal, N., Hunt, A., 2010. Study of fluidisation using electrical capacitance tomography. In: 7th International Conference on Multiphase Flow, Tampa, Florida, USA, 30 May–4 June.
Azzopardi, B.J., Abdulkareem, L.A., Sharaf, S., Abdulkadir, M., Hernandez-Perez, V., Ijioma, A., 2010. Using tomography to interrogate gas–liquid flow. In: 28th UIT Heat Transfer Congress, Brescia, Italy, 21–23 June.
Azzopardi, B.J., Do, H.K., Azzi, A., Hernandez-Perez, V., 2015. Characteristics of air/water slug flow in an intermediate diameter pipe. Exp. Therm. Fluid Sci. 60, 1–8.
Beggs, H.D., 1972. An Experimental Study of Two Phase Flow in Inclined Pipes (Ph.D. thesis). The University of Tulsa, Tulsa, OK.
Bhagwat, S.M., Ghajar, A.J.A.J., 2014. A flow pattern independent drift flux model based void fraction correlation for a wide range of gas–liquid two phase flow. Int. J. Multiphase Flow 59, 186–205.
Bolton, G.T., Korchinsky, W.J., Waterfall, R.C., 1998a. Calibration of capacitance tomography system for liquid–liquid dispersions. Meas. Sci. Technol. 9, 1797–1800.
Chisholm, D., 1973. Pressure gradient due to friction during the flow of evaporating two-phase mixtures in smooth tubes and channels. Int. J. Heat Mass Transfer 16, 347–358.
Clark, N.N., Flemmer, R.L., 1985. Predicting the holdup in two-phase bubble upflow and downflow using the Zuber and Findlay drift flux model. AIChE 31, 500–503.
Coddington, P., Macian, R., 2002. A study of the performance of void fraction correlations used in the context of drift-flux two-phase flow models. Nucl. Eng. Des. 215, 199–216.
Costigan, G., Whalley, P.B., 1997. Slug flow regime identification from dynamic void fraction measurements in vertical air–water flows. Int. J. Multiphase Flow 23, 263–282.
Crawford, T.J., 1983. Analysis of Steady State and Transient Two-Phase Flows in Downwardly Inclined Lines (Ph.D. thesis). Drexel University.
Da Silva, M.J., Thiele, S., Abdulkareem, L., Azzopardi, B.J., Hampel, U., 2010. High-resolution gas-oil two-phase flow visualization with a capacitance wire-mesh sensor. Flow Meas. Instrum. 21, 191–197.
Da Silva, M.J., Hampel, U., Arruda, L.V., do Amaral, C.E.F., Morales, R.E.M., 2011. Experimental investigation of horizontal gas–liquid slug flow by means of wire mesh sensor. J. Braz. Soc. Mech. Sci. Eng. XXXIII, 237–242.
Friedel, L., 1979. Improved friction pressure drop correlations for horizontal and vertical two-phase pipe flow. In: European Two Phase Flow Group Meeting, Ispra, Italy, paper E2.
Furukawa, T., Fukano, T., 2001. Effects of liquid viscosity on flow patterns in vertical upward gas–liquid two-phase flow. Int. J. Multiphase Flow 27, 1109–1126.
Govier, G.W., Aziz, K., 1972. Flow of Complex Mixtures in Pipes. Van-Nostrand-Reinhold, Princeton, NJ, USA.
Greskovich, E.J., Cooper, W.T., 1975. Correlation and prediction of gas–liquid holdups in inclined upflows. AIChE J. 21, 1189–1192.
Griffith, P., Two-Phase Flow in Pipes, 1962. In Special Summer Program. Massachusetts Institute of Technology, Cambridge, MA, USA.
Hanratty, T.J., Theofanous, T., Delhaye, J.-M., Eaton, J., McLaughlin, J., Prosperetti, A., Sundaresan, S., Tryggvason, G., 2003. Workshop on scientific issues in multiphase flow. Int. J. Multiphase Flow 29, 1042–1116.
Hasan, A.R., 1995. Void fraction in bubbly and slug flow in downward vertical and inclined systems. Soc. Petrol. Engrs. Prod. Facil. 10, 172–176.
Hasan, A.R., Kabir, C.S., 2010. Simplified two-phase flow modelling in wellbores. J. Petrol. Sci. Eng. 72, 42–49.
Hernandez-Perez, V., 2008. Gas–Liquid Two-Phase Flow in Inclined Pipes. University of Nottingham, PhD thesis.
Holt, A.J., 1996. Pressure Drop and Void Fraction in Narrow Channels. University of Nottingham, PhD thesis.
Huang, Z., Wang, B., Li, H., 2003. Application of electrical capacitance tomography to the void fraction measurement of two-phase flow. IEEE Trans. Instrum. Meas. 52, 7–12.
Hughmark, G.A., 1962. Holdup in gas–liquid flow. Chem. Eng. Prog. 58, 62–65.
Jayanti, S., Hewitt, G.F., 1992. Prediction of the slug-to-churn flow transition in vertical two-phase flow. Int. J. Multiphase Flow 18, 847–860.
Jowitt, D., Cooper, C.A., Pearson, K.G., 1984. The THETIS 80% blocked cluster experiment. Part 5: level swell experiment, AEEW-R 1767. In: AEEE Winfrith, Safety and Engineering Division, Winfrith UK.
Kokal, S.L., Stanislav, J.F., 1989. An experimental study of two phase flow in slightly inclined pipes II: liquid holdup and pressure drop. Chem. Eng. Sci. 44, 681–693.
Lockhart, R.W., Martinelli, R.C., 1949. Proposed correlation of data for isothermal two-phase, two-component flow in pipes. Chem. Eng. Prog. 45, 39–48.
Mandhane, J.M., Gregory, G.A., Aziz, K., 1974. A flow pattern map for gas-liquid flow in horizontal pipes. Int. J. Multiphase Flow 1, 537–553.
Mukherjee, H., 1979. An Experimental Study of Inclined Two-Phase Flow (Ph.D. thesis). the University of Tulsa, Tulsa, OK.
Neal, L.G., Bankoff, S.G., 1965. Local parameters in cocurrent mercury–nitrogen flow: Parts I and II. AIChE J. 11, 624–635.
Nguyen, V.T., 1975. Two Phase Gas–Liquid Concurrent Flow: An Investigation of Holdup, Pressure Drop and Flow Patterns in a Pipe at Various Inclinations (Ph.D. thesis). The University of Auckland, Auckland.
Nichols, C.R., 1965. A Study of Vertical Flow of An Air–Water Mixture (Ph.D. thesis). University of Maryland.
Nicklin, D.J., Wilkes, J.O., Davidson, J.F., 1962. Two-phase flow in vertical tubes. Trans. Inst. Chem. Engrs. 156, 61–68.
Omebere-Iyari, N.K., Azzopardi, B.J., 2007. A study of flow patterns for gas/liquid flow in small diameter tubes. Chem. Eng. Res. Des. 85, 180–192.
Omebere-lyari, N.K., Azzopardi, B.J., 2000. Links across flow-patterns in gas–liquid flow in vertical pipes. In: Paper presented at the 2nd Japanese-European Two-Phase Group Meeting, Tsukuba, 25–29 September.
Orkiszewski, J., 1967. Predicting two-phase pressure drops in vertical pipe. J. Petrol. Technolol. 19, 829–838.
Pereyra, E., Torres, C., 2005. FLOPATN—Flow Pattern Prediction and Plotting Computer Code. The University of Tulsa, Tulsa, OK.
Prasser, H.M., Misawa, M., Tiseanu, I., 2005. Comparison between wire-mesh sensor and ultra-fast X-ray tomograph for an air-water flow in a vertical pipe. Flow Meas. Instrum. 16, 73–83.
Sharaf, S., van der Meulen, G.P., Agunlejika, E.O., Azzopardi, B.J., 2016. Structures in gas–liquid churn flow in a large diameter vertical pipe. Int. J. Multiphase Flow 78, 88–103.
Sokolov, V.N., Davydov, I.V., Domanskii, I.V., 1969. Gas content in tubular bubbling reactors of the displacement type. J. Appl. Chem. USSR 42.
Spedding, P.L., Spence, D.R., Hands, N.P., 1990. Prediction of holdup in two-phase gas–liquid inclined flow. Chem. Eng. J. 45, 55–74.
Su, C., Metcalfe, R.W., 1997. Influences of liquid properties on gas entrainment at the bottom of a fixed bubble. In: Proceedings of the ASME Fluids Engineering Division Summer Meeting, Vancouver, pp. 1–7.
Taitel, Y., Barnea, D., Dukler, A.E., 1980. Modelling flow pattern transitions for steady upward gas–liquid flow in vertical tubes. AIChE J. 26, 345–354.
van der Meulen, G.P., 2012. Churn–Annular Gas–Liquid Flows in Large Diameter Vertical Pipes (Ph.D. thesis). University of Nottingham.

Wallis, G.R., 1969. One-Dimensional Two-Phase Flow. McGraw-Hill, New York.
Waltrich, P.J., Falcone, G., Barbosa, J.R., 2013. Axial development of annular, churn and slug flows in a vertical tube. Int. J. Multiphase Flow 57, 38–48.
Wang, S.J., Dyakowski, T., Xie, C.G., Williams, R.A., Beck, M.S., 1995. Real time capacitance imaging of bubble formation at the distributor of a fluidized bed. Chem. Eng. J. 56, 95–100.
Wang, K., Bai, B., Cui, J., Ma, W., 2012. A physical model for huge wave movement in gas–liquid churn flow. Chem. Eng. Sci. 79, 19–28.
Wangjiraniran, W., Aritomi, M., Kikura, H., Motegi, Y., Prasser, H.M., 2005. A study of non-symmetric air water flow using wire mesh sensor. Exp. Therm. Fluid Sci. 29, 315–322.
Woldesemayat, M.A., Ghajar, A.J., 2007. Comparison of void fraction correlations for different flow patterns in horizontal and upward inclined pipes. Int. J. Multiphase Flow 33, 347–370.
Xie, C.G., Huang, S.M., Hoyle, B.S., Thorn, R., Lenn, C., Snowden, D., Beck, M.S., 1992. Electrical capacitance tomography for flow imaging: system model for development of image reconstruction algorithms and design of primary sensors. IEE Proc. G 139, 89–97.
Yamazaki, Y., Yamaguchi, K., 1979. Characteristics of two-phase downflow in tubes: flow pattern, void fraction and pressure drop. J. Nucl. Sci. Technol. 16, 245–255.
Yang, W.Q., 1996. Calibration of capacitance tomography system: a new method for setting measurement range. Meas. Sci. Technol. 7, 863–867.
Yijun, J., Rezkallah, K., 1993. A study on void fraction in vertical co-current upward and downward two-phase gas–liquid flow. I. Experimental results. Chem. Eng. Commun. 126, 221–243.